ADVANCED MATERIALS
www.advmat.de

Flash Thermal Shock Synthesis of Heterostructured Transition Metal Dichalcogenides and Carbides in Milliseconds

*Euichul Shin, Dong-Ha Kim, Mingyu Sagong, Jacob Choe, Seo Hak Park, Jaewan Ahn, Jong Won Baek, Minhyun Kim, Sungyoon Woo, Yujang Cho, Seon-Jin Choi, Sang-Joon Kim, Jong Min Yuk, Ju Li, Sung-Yool Choi, and Il-Doo Kim**

Transition metal dichalcogenides (TMDs) offer remarkable potential for next-generation functional devices, but achieving ultrafast synthesis with precise structural and phase control under ambient conditions remains a significant challenge. Here, ultrafast photothermal annealing assisted by graphene oxide is introduced for precise phase control of TMDs forming a heterostructure. This process reaches adjustable temperatures between 1 768 and 3 162 K within 10 ms, featuring rapid kinetics, enabling the synthesis of various metastable nanomaterials in ambient air. The TMDs form directly from precursors above 1 700 K, while temperatures above 2 300 K induce carbothermic reactions, producing metastable transition metal carbides (TMCs) and core@shell heterostructures (TMC@TMD and TMC@carbon). Introducing seed materials like single metals, metal oxides, and multielement/high-entropy alloys enables the formation of core(seed)@shell (TMD) heterostructures. The resulting composites demonstrated significantly enhanced catalytic performance in gas sensing and hydrogen production. This robust and versatile photothermal annealing method holds broad potential for designing advanced heterostructure-engineered TMD and/or TMC composites tailored for targeted applications.

1. Introduction

Transition metal dichalcogenides (TMDs) have been proposed as promising nanomaterials due to their inherent high surface-to-volume ratio, catalytic activity at edge sites, and tunable electrical and chemical properties.[1,2] The ways to enhance the activity of TMDs are classified by tuning inactive basal planes and improving the active edges.[3] One way to enhance the activity of TMDs is to confine their lateral dimensions to the nanometer regime, which maximizes the number of active edge sites. In addition, atomic structure modulation of TMDs, such as the introduction of curvature, which induces vacancy formations and phase transitions, has demonstrated substantial enhancements in basal planes.[4,5] Although these modifications improve catalytic activity, the spontaneous deactivation of thermodynamically unstable TMDs and inefficient synthetic processes remain

E. Shin, M. Sagong, J. Choe, J. Ahn, J. W. Baek, M. Kim, S. Woo, Y. Cho, J. M. Yuk, I.-D. Kim
Department of Materials Science and Engineering
Korea Advanced Institute of Science and Technology
291 Daehak-ro Yuseong-gu, Daejeon 34141, Republic of Korea
E-mail: idkim@kaist.ac.kr

D.-H. Kim
Department of Materials Science & Chemical Engineering
Hanyang University-ERICA
55 Hanyangdaehak-ro, Sangnok-gu, Ansan, Gyeonggi-do 15588, Republic of Korea

S. H. Park, S.-Y. Choi
School of Electrical Engineering
Korea Advanced Institute of Science and Technology (KAIST)
291 Daehak-ro, Yuseong-gu, Daejeon 34141, Republic of Korea

The ORCID identification number(s) for the author(s) of this article can be found under https://doi.org/10.1002/adma.202419790

DOI: 10.1002/adma.202419790

S.-J. Choi
Division of Materials of Science and Engineering
Hanyang University
222 Wangsimni-ro, Seongdong-gu, Seoul 04763, Republic of Korea

S.-J. Kim
Department of Materials Science and Engineering
Chungnam National University
Daejeon 34134, Republic of Korea

I.-D. Kim
Membrane Innovation Center for Anti-Virus & Air-Quality Control
KI Nanocentury
KAIST, 291 Daehak-ro Yuseong-gu, Daejeon 34141, Republic of Korea

J. Li
Department of Nuclear Science and Engineering
Massachusetts Institute of Technology
77 Massachusetts Avenue, Cambridge, MA 02139, USA

J. Li
Department of Materials Science and Engineering
Massachusetts Institute of Technology
77 Massachusetts Avenue, Cambridge, MA 02139, USA

challenging. To overcome these obstacles, van der Waals (vdW) force-based heterostructure construction has emerged as a promising strategy. This approach not only restricts aggregation but also tailors the mechanical and chemical properties of TMDs to meet application-specific requirements by leveraging the synergistic effects between TMDs and their supports.[6] For instance, the nanoparticle with encapsulation of TMD (i.e., core@shell heterostructure) effectively regulates aggregation of TMDs owing to vdW forces and improves the catalytic activity via high curvatures of TMDs.[7] The heterostructures of TMDs with vdW insulator chromium oxychloride (CrOCl) effectively modulated the dominant carrier type from electrons to holes due to strong vdW interfacial coupling.[8] However, conventional TMD heterostructure construction requires transportation of support or parent materials into TMDs. In addition, these synthetic conditions often involve high pressure, high temperature for prolonged periods, a specific gas-contained environment, and inert atmospheric protection. These slow and energy-intensive procedures not only hinder energy efficiency but reduce the activity of TMDs due to an excessive supply of sources and the limited thermodynamic stable combination of heterostructures.

Recently, ultrafast thermal treatment techniques have opened new avenues for creating non-equilibrium conditions for energy-efficient high-temperature syntheses, such as direct resistive joule heating,[9,10] laser annealing,[11,12] sparking,[13] and light-based photothermal heating.[14–16] The formation of metastable phases is inherently governed by the interaction between thermodynamics and kinetics during ultrafast heating and cooling.[17] Furthermore, rapid thermal dissipation suppresses phase equilibrium, enabling the retention of non-equilibrium structures, which induce metastable states.[18] In this regard, these ultrafast techniques have been advantageous for engineering metastable nanomaterials, including phase-controlled transition metal carbides,[19] high-entropy alloys, and ceramics.[12] Among non-equilibrium thermal systems, intensive pulsed light-derived flash-thermal shock (FTS) is particularly attractive given it applicability over large areas, does not require use of conductive materials (i.e., carbon), and can induce steep temperature gradients of up to the order of 3000 K within milliseconds.[20,21] However, despite their advantages, FTS systems, while having been demonstrated in synthesizing catalyst design, remain limited in achieving precise structural and phase control in complex nanomaterials, particularly in heterostructure engineering.[22,23]

Here, we demonstrate a highly effective synthetic protocol for creating heterostructure- and phase-controlled TMDs and transition metal carbides (TMCs) through the ultrafast photothermal effect of graphene oxides (GO) using non-equilibrium FTS. The GO, having high photothermal efficiency, served as an essential auxiliary photothermal agent due to its numerous light absorption sites and continuous light absorption over its progressively decreasing bandgap as a result of the concurrent formation of reduced GO (rGO).[15] This photothermal effect drives ultrafast heating ($\approx 10^6$ K s^{-1}) and cooling rates ($\approx 10^5$ K s^{-1}), enabling the synthesis of metastable TMC and TMDs, as well as core@TMDs shell heterostructures by controlling the photothermal temperatures ranging from 1700 to 3200 K. Importantly, we prepared core@shell heterostructures with TMDs shells (as well as graphitic carbon shells), wherein the core nanoparticles (NPs) could be transition metal carbides (e.g., α-MoC), metal oxides (e.g., WO_3, Co_3O_4, In_2O_3, Fe_3O_4), single-metals (e.g., Au, Ag), or multielement/high-entropy alloys (e.g., PtPdIrRuAu, PtPdIrRuAuCoSnNiFeCu). The versatility of this synthetic route indicates that designing highly active metastable nanomaterials, including TMC, TMD, and core@shell NPs with customizable core materials tailored for specific applications is now a viable concept. By combining ultrafast photothermal effects with precise structural control, this approach overcomes conventional synthesis limitations and establishes a versatile platform for designing functional nanomaterials tailored to catalysis, sensing, and energy conversion applications.

2. Results and Discussion

2.1. Synthesis and Phase Transformation of TMDs and TMCs by Flash-Thermal Shock

To synthesize rGO-supported TMDs and TMCs, we first prepared aqueous GO solutions containing precise amounts of transition metal precursors. Stable GO solutions are easily produced due to their similar hydrophilicity and negative charges (Figure S1, Supporting Information).[24] The as-prepared solution was drop-casted on a glass substrate and dried at 353.15 K. Subsequently, a burst of intense pulsed light (IPL) irradiated the coated glass slide to induce FTS (**Figure 1a**). For reference, IPL-treated pristine GO reached 2970 K from room temperature, with an ultrafast heating rate of $\approx 7.50 \times 10^6$ K s^{-1} for 10 ms duration (Figure S2, Supporting Information). By leveraging the high photothermal temperatures and rapid kinetics of FTS, we synthesized a variety of metastable nanomaterials through phase transition, encapsulation, and carbothermic reactions. The TMDs exhibit significant physicochemical differences depending on their phase (e.g., 1T and 2H), with their properties further tuned through interactions with encapsulated core materials and curvature-induced modifications (Figure 1b,c). Additionally, the ultrafast carbothermic reaction enables synthesis of ultra-hard and strong metastable TMCs, expanding the scope of achievable heterostructures (Figure 1d).[19] As proof of concept, we showcase the synthesis of phase-controlled MoS_2, metastable α-MoC, and combined core@shell (α-MoC@MoS_2) nanoparticles using molybdenum precursors (ammonium tetrathiomolybdate (ATTM), $(NH_4)_2MoS_4$), as well as 1T-WS_2, metastable W_2C, and W_2C@graphitic carbon by tungsten precursors (ammonium tetrathiotungstate (ATTT), $(NH_4)_2WS_4$). The selection of Mo- and W-based dichalcogenides and carbides is driven by their versatility, making them promising candidates for designing functional nanomaterials with tailored physicochemical properties, which are ideally suited for advanced catalysis and sensing applications.[1,6] Importantly, although the temperature generated by FTS (i.e., "photothermal temperature") is significantly higher than the decomposition temperature (≈700 K) of GO at thermodynamic equilibrium,[25] the extremely short annealing time (<10 ms) allows the structure of GO to be preserved while partially reducing it into rGO (Figures S3 and S4, Supporting Information). Using the IR system, we quantified the photothermal effect induced in the ATTM-containing sample and the ATTT-containing sample, which had varying amounts of photothermal agents (i.e., GO). The photothermal

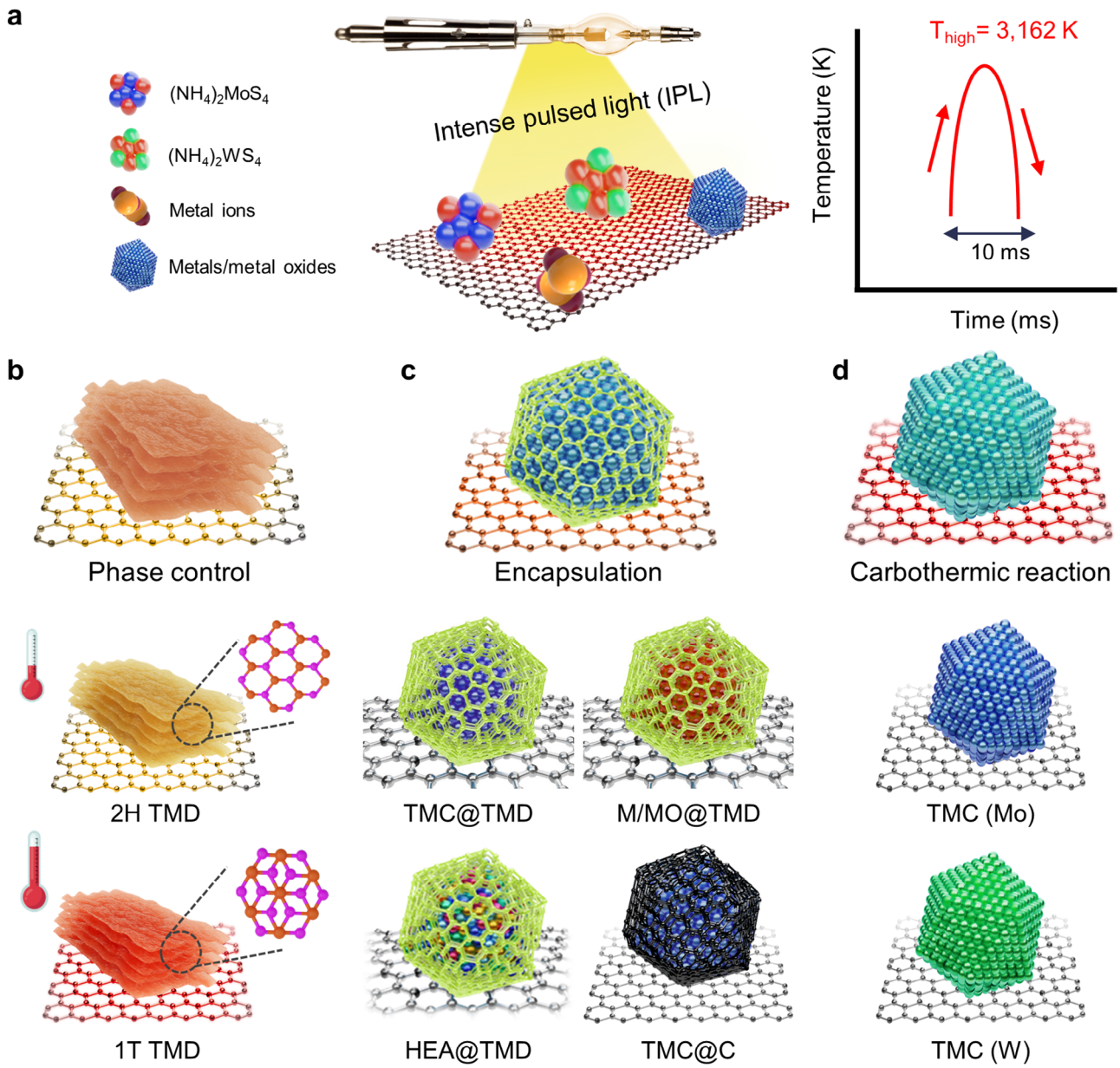

Figure 1. Schematic of the heterostructure engineering of TMDs and TMCs. a) Schematic diagram of the preparation of TMDs and TMCs by Intense pulsed light. A photothermal effect is induced immediately at GO, reaching up to 3162 K within 10 ms with a heating rate of 9.7×10^5 K s^{-1} and cooling rate of 2.3×10^5 K s^{-1}, which are suitable for metastable nanomaterial synthesis. b) Phase-controlled TMD containing 2H phase and metastable 1T phase. c) Encapsulation of TMD or graphitic carbon. The core materials are composed of TMC, single-metal (M), metal oxide (MO), and high-entropy alloy (HEA). d) Transition metal carbides through a carbothermic reaction of GO.

temperature could be controlled from 1768 up to 3162 K by increasing the GO ratio, while the reaction time remained fixed at ≈10 ms, consistent with the irradiation duration (**Figure** 2a,d). Mo- and W-based materials were uniformly synthesized on the rGO substrate via flash-thermal conversion of ATTM and ATTT, respectively (Figure S5, Supporting Information). We experimentally investigated the FTS-induced phase transformation mechanism, establishing that the photothermal temperature is a key parameter for the controlled synthesis of TMDs and TMCs, critically determining the selective conversion behavior of ATTM and ATTT, while the total precursor amounts also played a significant role (Note S1, Supporting Information). To further elucidate the precise control for the synthesis of TMDs and TMCs, we selected different precursor contents while maintaining a constant irradiated energy density for case studies. Figure 2a–c shows the various ratios of GO:ATTM under constant irradiation by FTS (10 J cm^{-2}). Despite the same irradiation energy, the photothermal agents controlled the photothermal temperatures, reaching 1768, 2369, and 2519 K (Figure 2a). The FTS-derived Mo-based materials exhibited distinct X-ray diffraction (XRD) patterns. The XRD data revealed the presence of TMDs, such as MoS_2 (PDF# 37–1492), and metastable TMCs, including molybdenum carbide

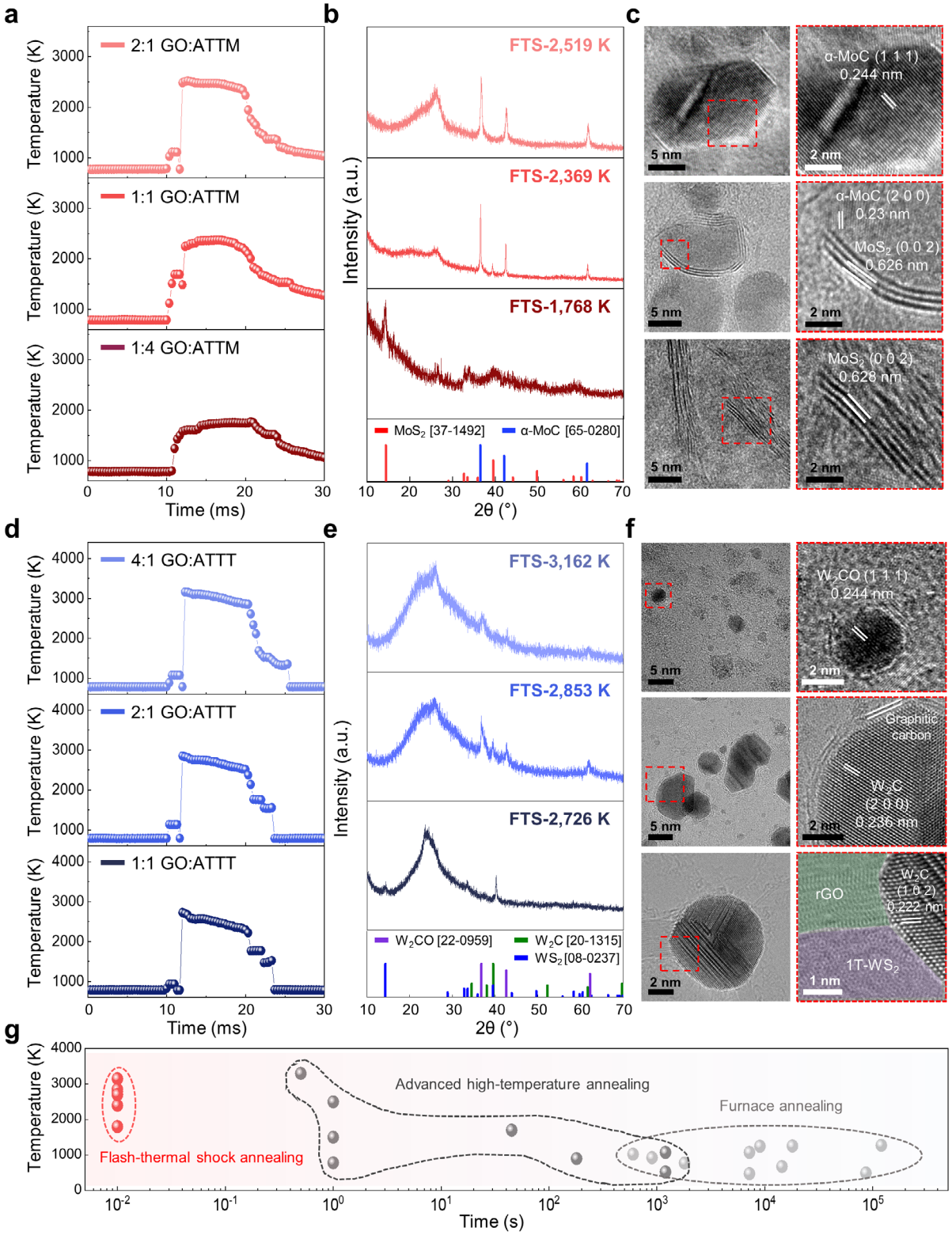

Figure 2. Temperature curves and Characterization of TMDs and TMCs. a) Temperature profile of ATTM contained GO with irradiation energy of 10 J cm^{-2}. The GO:ATTM indicated the weight ratio between GO and ATTM. b,c) XRD patterns (b) TEM images (c) of Mo-based materials after FTS. The number X of FTS–X K denotes a photothermal temperature of FTS. d) Temperature-curve of ATTT contained GO with irradiation energy of 25 J cm^{-2}. e,f) XRD patterns (e) and TEM images (f) of W-based materials after FTS. g Time and temperature comparison of the synthesis of TMDs and TMCs by FTS with advanced high-temperature annealing and conventional furnace annealing. The exact temperature and time are summarized in Table S1 (Supporting Information).

(α-MoC, PDF# 65–0280) (Figure 2b). The TMCs were synthesized at higher photothermal temperatures than TMDs due to the carbothermic reaction. Thus, the resulting materials could be selectively synthesized by adjusting the photothermal temperatures. Note that the broad diffraction peak at ≈25° is attributed to the (002) plane of rGO, while the peaks ≈26–27° are attributed to MoO_2 and WO_2, resulting from surface oxidation.[26] The photothermal annealing at 1768 K (FTS−1768 K), which is insufficient to trigger the carbothermic reaction of GO, led to the decomposition of ATTM into MoS_2 rather than α-MoC. Interestingly, it should be noted that α-MoC could only be obtained at photothermal temperatures above 2300 K since this threshold temperature is sufficient to trigger the carbothermic reaction of GO.[19]

To investigate the surface characteristics of molybdenum compounds synthesized through FTS, we analyzed the FTS-treated samples with X-ray photoelectron spectroscopy (XPS). The XPS peak fitting in the Mo 3d region revealed characteristic peaks assigned to Mo^{2+}, Mo^{4+}, and Mo^{5+} located at 228.2, 229.0, 229.7, and 230.3 eV, respectively, each corresponding to the Mo $3d_{5/2}$ of Mo^{2+}, Mo^{4+} (2H-MoS_2), Mo^{4+} (α-MoC and 1T-MoS_2),[10] Mo^{5+} (MoO_x) with doublet at 3.15 eV (Figure S6, Supporting Information).[27,28] While both the Mo^{2+} and Mo^{4+} species are associated with α-MoC, the convoluted Mo^{4+} peak also contains a sub-peak corresponding to the MoS_2 phase. As the relative amount of ATTM increased, the dominant peaks shifted from those of Mo^{2+} to Mo^{4+}, indicating a greater proportion of MoS_2 formation. The spin-orbit separation between S $2p_{1/2}$ and S $2p_{3/2}$ was measured at 1.15 eV, indicating the presence of the S^{2-} species. The peaks at binding energies of 161.9 and 162.6 eV in the S $2p_{3/2}$ region were attributed to MoS_2 (1T and 2H phases, respectively) or terminal S_2^{2-} sites of MoS_2. In addition, the peak with the binding energy of 163.4 eV for S $2p_{3/2}$ is associated with unsaturated sulfur atoms, such as apical S^{2-} or bridging S_2^{2-} ions (Figure S6, Supporting Information).[28,29] Thus, we confirmed that the phase-controlled MoS_2 was synthesized on rGO by tuning the photothermal temperatures via FTS (Figure S7, Supporting Information). This result aligns with the higher energy required for the formation of metastable 1T-MoS_2. In addition, Raman studies were conducted to further characterize the surface of FTS-derived TMDs. The vibrational bands were located at 155, 200, 277, 344, 404, and 430 cm^{-1}, corresponding to the J_1, J_2, E^1_g, J_3, E^1_{2g} and A_{1g} modes of 1T-MoS_2, respectively. Two characteristic peaks at 380.1 and 404.7 cm^{-1} were associated with 2H-MoS_2, corresponding to the in-plane optical (E^1_{2g}) and out-of-plane vibration (A_{1g}) modes (Figure S7, Supporting Information).[30,31] The FTS−1768 K and FTS−2519 K samples exhibited distinct peaks, corresponding to 2H-MoS_2 and 1T-MoS_2, respectively, while the FTS−2369 K sample showed both phases of MoS_2. These results confirmed that the precise control of photothermal temperature via the FTS process enables the fine-tuning of phase ratio in MoS_2, simultaneously facilitating the synthesis of the thermodynamic unstable and highly active 1T-MoS_2.

Transmission electron microscopy (TEM) was conducted to characterize the morphology of the TMDs and TMCs on rGO. The molybdenum compounds on the surface of rGO were confirmed by high-resolution TEM (HRTEM) analysis by calculating the lattice fringes of α-MoC and MoS_2 (Figure 2c). The interplanar distances of 0.230 and 0.244 nm correspond to the (200) and (111) planes of α-MoC, respectively. In addition, the layered MoS_2 was identified by measuring the lattice fringes, which corresponded to (002) planes. The heterostructure of Mo-based TMDs and TMCs exhibited various morphologies with uniform distributions (Figures S8–S10, Supporting Information). The heterostructure was confirmed to be a core@shell structure comprising an α-MoC core and MoS_2 shell (α-MoC@MoS_2). The ATTM was decomposed and sequentially synthesized into MoS_2, then to sulfur-deficient MoS_2, and then to molybdenum carbides (Note S1, Supporting Information). Under sufficient temperatures to induce the carbothermic reaction, the sulfur atoms were removed by sublimation, and the remaining molybdenum reacted with carbon to produce α-MoC.[32] Based on this understanding, the carbothermic reaction occurs at the interface between the TMDs and rGO. In this process, α-MoC is formed by the adjacent layer of MoS_2 to the rGO, while the remaining layers of MoS_2 structure, result in the core@shell α-MoC@MoS_2 configuration.

Furthermore, similar to the synthesis of molybdenum compounds, the stepwise conversion of ATTT to WS_2, W_2C, and then to W_2CO was progressively observed as photothermal temperature increased from 2726 to 3162 K (Figure 2d; Note S2, Supporting Information). Given that the formation energy of tungsten carbides is higher than that of molybdenum carbides, 2.5-fold higher irradiation energy (25 J cm^{-2}) was applied, resulting in higher photothermal temperatures than those achieved with ATTM-contained GO.[33] The high energy input and ultrafast kinetics of FTS made it possible to bypass the formation of thermodynamically stable WC and result in the synthesis of metastable W_2C, and W_2CO on rGO (Figure S11, Supporting Information).[34] The tungsten disulfide (WS_2, PDF# 08–0237), tungsten carbide (W_2C, PDF# 20–1315), and tungsten oxycarbide (W_2CO, PDF# 22–0959) were confirmed from the XRD patterns (Figure 2e). In the case of ATTT-containing samples, the resultant material exhibited a W^{2+} peak associated with both the W_2CO and W_2C phases. The W^{4+} peak showed a downshift that is attributed to weaker binding between W and S (FTS−2726 K and FTS−2853 K) compared to C and O (FTS−3162 K). The W^{6+} peak indicates WO_x species formed by surface oxidation in the air (Figure S12, Supporting Information). The Raman spectra of the WS_2 exhibited distinctive peaks of 1T-WS_2 at 133.3, 276.3, 332.1, and 433.2 cm^{-1}, corresponding to J_1, J_2, E^1_{2g}, and A_{1g}, respectively, due to the synthesis of metastable 1T-WS_2 at high photothermal temperatures (>2700 K) (Figure S11, Supporting Information).[35] Moreover, the W-based TMDs and TMCs were synthesized on the surface of rGO with uniform distributions (Figures S13–S15, Supporting Information). The distances of the lattice fringe of W_2C and W_2CO were measured at 0.236 and 0.244 nm, which correspond to those of the (111) and (200) planes, respectively (Figure 2f). Similar to MoC@MoS_2, core@shell heterostructures were confirmed with a combination of a W_2C core with a graphitic carbon shell (W_2C@C). These intense irradiations induced the predominant conversion into tungsten carbides, and the high temperature (>2800 K) facilitated the excessive carbothermic reaction of GO, resulting in the formation of a graphitic carbon shell (W_2C@C).[19] Altogether, our FTS-based method for synthesizing TMDs and TMCs composites offers significant advantages based on the capability to higher temperatures and faster heating rates compared to other

reported methods (Figure 2g; Table S1, Supporting Information). In context, conventional annealing methods using furnaces usually operate at temperatures of ≈1000 K with a processing time of several hours to synthesize TMDs and TMCs composites. Also, high-temperature annealing by rapid Joule heating was recently reported to have achieved ≈3000 K within 500 ms.[19] In comparison, the FTS method achieved a temperature higher than 3000 K in just 10 ms, which is more energy efficient and facilitates the synthesis of metastable materials (Notes S3–S5, Supporting Information). These results confirm that the FTS process offers significant advantages for diverse structural control, particularly in the synthesis of core@shell NPs. These structures not only benefit from the heterostructural advantages, such as van der Waals interactions between the core and shell but also provide structural enhancements, including the shielding effect of the core and strain effects induced by the curvature of the shell.[5–7] In the synthesis of core@shell structure, the core additives, such as Ag, Au, and SiO_2, serve as seed materials for synthesizing TMDs owing to lower interface energy.[36] The three major considerations for the synthesis of the core@TMDs shell heterostructures are (1) interface formation energy, (2) synthesis conditions, and (3) morphology of the core materials. Conventional synthetic methods (e.g., CVD) primarily rely on thermodynamically favorable nucleation sites, often leading to selective deposition at low interface formation energy sites, thereby limiting encapsulation at high-energy interfaces.[36] Additionally, prolonged reaction times in conventional synthesis could cause excessive lateral growth, resulting in winged or flower-like TMD structures due to kinetically trapped intermediate states.[37] The graphitic carbon encapsulation through carbothermal shock (CTS) was confirmed in various transition metal carbides.[19] The carbothermic reduction process, driven by the ultrafast and high-energy input of CTS (≈3000 K), resulted in the formation of transition metal carbides with conformal graphitic carbon shells. In this regard, FTS provides ultrafast and high-energy photothermal heating, not only enabling non-equilibrium encapsulation even at high interface formation energy sites, but also achieving conformal encapsulation. Thus, the FTS-based annealing provides sufficient energy to form TMDs on various seed materials and simultaneously synthesizes metastable NPs, which serve as seed materials. Moreover, the rapid heating and cooling of the FTS process effectively eliminates artifacts, such as winged or flower-like core@shell structures caused by excessive growth of TMD.[38] In this study, we demonstrated the broad applicability of the FTS synthesis approach for core@TMDs shell NPs, wherein the non-carbide core materials, including single-metals (Ag, Au), multielement/high-entropy alloys (PtPdIrRuAu, PtPdIrRuAuCoSnNiFeCu), and transition metal oxides including tungsten oxide (WO_3), cobalt oxide (Co_3O_4), indium oxide (In_2O_3), and iron oxide (Fe_2O_3) were considered. **Figure 3a** depicts the synthetic process of core@TMDs shell heterostructured NPs on the surface of rGO. In a standard protocol, the Mo, W precursor contained GO solutions (1:1 GO:ATTM (ATTT)) were prepared by incorporating 1 wt% of seed material. Even after the addition of seed material, the photothermal temperatures remained consistently above 2000 K, facilitating the nucleation and growth of TMDs on the surface of the core materials (Figure S16, Supporting Information). As case studies, we demonstrated the feasibility of the synthesis of TMDs on single-metal and metal oxide NPs, including Au@MoS_2 (Figure 3b) and In_2O_3@MoS_2 (Figure 3c). Other case studies of single-metal (Ag@MoS_2) and metal oxides (WO_3@MoS_2, Co_3O_4@MoS_2, Fe_2O_3@MoS_2) were also confirmed (Figure S17, Supporting Information). Moreover, the other case of TMDs, WS_2, also synthesized on single-metals (Ag@WS_2, Au@WS_2) and metal oxides (WO_3@WS_2, Co_3O_4@WS_2, In_2O_3@WS_2, Fe_2O_3@WS_2) NPs (Figure S18, Supporting Information). The outer shell of the TMDs was clearly revealed through energy-dispersive X-ray spectroscopy (EDS) mapping, highlighting its distinct structure. In addition, the lattice fringes, measuring ≈0.62 nm, further confirmed the presence of TMDs. Recently, the high-entropy alloy (HEA) NPs were synthesized on the rGO by FTS,[21] where the HEA NPs can provide nucleation and growth sites of TMDs similar to other single-metals and metal oxides by overcoming the thermodynamic limitation using FTS. Thus, PtPdIrRuAu@MoS_2 and PtPdIrRuAuCoSnNiFeCu@MoS_2 NPs were synthesized on rGO after FTS (Figure 3d,e; Figures S19–S21, Supporting Information). These metastable nanosized core@shell NPs were synthesized through ultrafast ramping kinetics, overcoming thermodynamic limitations with heating rates of ≈10^6 K s^{-1} and cooling rates of ≈10^5 K s^{-1}. These case studies demonstrated the formation of core@shell heterostructures, where the MoS_2 or WS_2 shell encapsulated the core materials, highlighting the versatility of FTS-based heterostructure engineering.

2.2. Applications: Chemical Gas Sensors and Hydrogen Evolution Catalysis

The unique FTS synthesis protocol combining GO enabled fabrication of previously challenging engineered heterostructures, such as highly active α-MoC@MoS_2 and metastable W_2C, W_2CO with distinct morphologies on rGO. To demonstrate the catalytic performance and the practical feasibility of heterostructure/phase-controlled synthesis of TMDs and TMCs on rGO, we evaluated their chemiresistive gas sensing performance and explored their electrocatalytic applications. For consistency, the samples are referred to by their compositions as characterized instead of their synthetic conditions (for instance, "α-MoC_MoS_2/rGO" indicates the sample with α-MoC and 1T-MoS_2 NPs on rGO, synthesized by FTS at 2519 K in a precursor ratio of 2:1 GO to ATTM). The rGO interacted with gas molecules on the surface through chemiresistive reactions, and the molybdenum compounds (e.g., α-MoC, MoS_2) acted as sensitizers toward target gas molecules (NO_2).[39,40] Detection in the low parts-per-million (ppm) range is particularly crucial, as it aligns with the permissible exposure limit for nitrogen dioxide (NO_2) set by the United States Occupational Safety and Health Administration (OSHA) at 1 ppm.[41] Therefore, the development of highly sensitive materials is essential to ensure accurate detection and safety compliance. The gas sensors were fabricated by coating a homemade Al_2O_3 substrate patterned with Au electrodes with sensing material (**Figure 4a**). The sensing performances of rGO, α-MoC_MoS_2/rGO, α-MoC@MoS_2/rGO, and MoS_2/rGO were evaluated after the sensors were exposed to 5 ppm of NO_2 with different relative humidity (RH), 15, 55, and 80%, respectively (Figure 4b). The water molecules enhanced

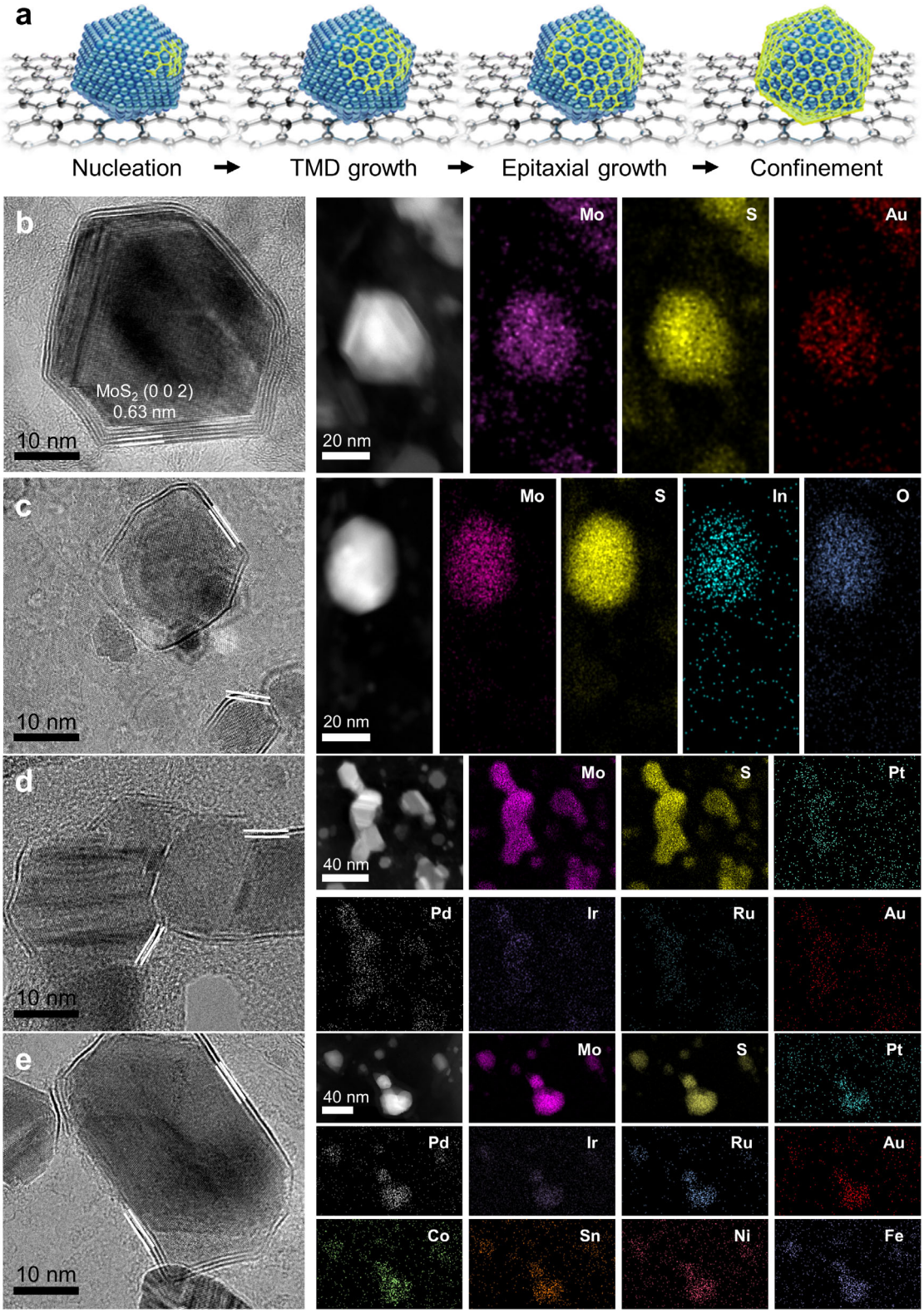

Figure 3. Core@TMDs heterostructured nanoparticle synthesis by FTS. a) Schematic illustration of synthesizing core@TMD shell heterostructured NPs on rGO. b–e) HRTEM, STEM, and EDS mapping images of Au@MoS_2 (b), In_2O_3@MoS_2 (c), PtPdIrRuAu@MoS_2 (d), and PtPdIrRuAuCoSnNiFeCu@MoS_2 (see also Figure S20 (Supporting Information), Cu) (e).

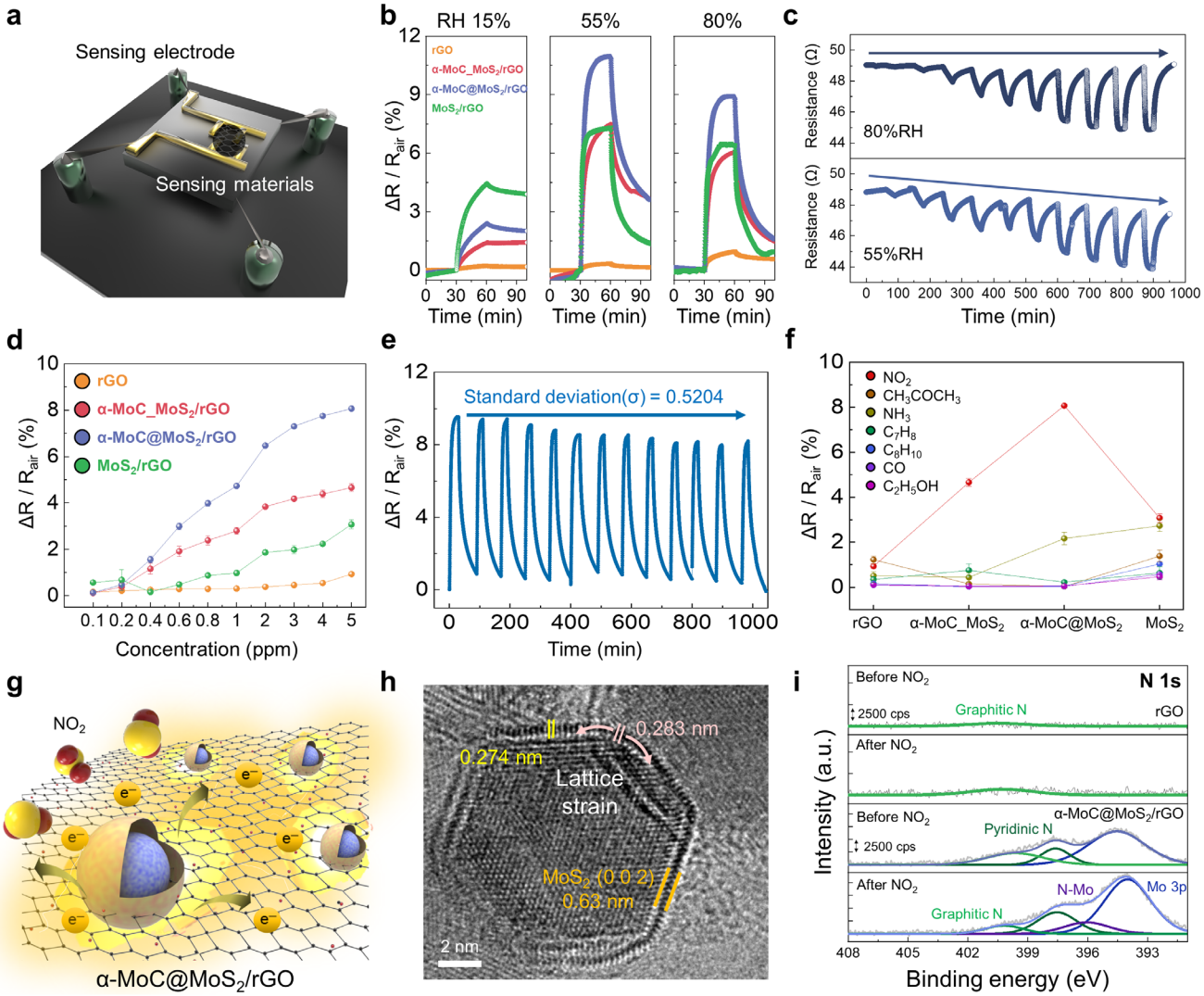

Figure 4. Gas sensing performance of TMDs and TMCs on rGO. a) Schematic illustration of room temperature operating gas sensor. b) NO_2 sensing performance under 15, 55, 80%RH of α-MoC@MoS_2/rGO. c) Dynamic responses for α-MoC@MoS_2/rGO with 55, 80% RH. d) Dynamic gas sensing performance of rGO, α-MoC_MoS_2/rGO, α-MoC@MoS_2/rGO, and MoS_2/rGO. e) Cyclic performance toward 5 ppm NO_2 of α-MoC@MoS_2/rGO. f) Selective sensing results of rGO samples. g) Schematic illustration for sensing mechanism of NO_2 and α-MoC@MoS_2/rGO. The black honeycomb substrate, blue core, and yellow shell indicate rGO, α-MoC, and MoS_2, respectively. h) TEM image of α-MoC@MoS_2/rGO, which indicated lattice strain of MoS_2. i) XPS spectra of N 1s for α-MoC@MoS_2/rGO and rGO in NO_2 exposure.

the sensing performance of rGO due to the ionization of surface functional groups, in which the anionized groups act as hole traps that increase the response.[42,43] However, excessive accumulation of water molecules on the surface may inhibit the interaction between the gases and the surface or result in competitive adsorption toward the target gases.[44,45] The response of pristine rGO increased under humid conditions, rising from 0.22 to 0.35 and 0.97 at RH levels of 15%, 55% and 80%, respectively. For rGO with MoS_2 and/or α-MoC, the response further improved, increasing from 1.41 to 7.49 and 6.05 (α-MoC_MoS_2/rGO), from 2.38 to 10.93 and 8.88 (α-MoC@MoS_2/rGO), and from 4.42 to 7.32 and 6.39 (MoS_2/rGO) (Figure S22, Supporting Information). For all types of rGO, sensitivity improved with higher humidity. Notably, α-MoC@MoS_2/rGO exhibited 31.2 and 9.2-fold improved NO_2 sensing performance toward 5 ppm compared to pristine rGO at 55 and 80% RH, respectively. Note that although the 55% RH condition resulted in a higher response, the poor recovery behavior of the sensor prohibits its long-term operation and reliability. We determined the optimized sensing material synthesized by FTS is α-MoC@MoS_2/rGO under 80% RH conditions, considering both the sensitivity and recovery characteristics of the sensor (Figure 4c). There are several factors that could explain the enhanced sensing behavior of α-MoC@MoS_2/rGO compared to pristine rGO. The layered water molecules effectively enhanced the mobility of electrons between the NO_2 and rGO, inducing high recovery properties under room temperature. Also, the curved MoS_2 induces sulfur vacancies due to their lattice strain, which improves the activity for gas absorption.[46] In addition, the van der Waals layers of α-MoC and MoS_2 could provide a pathway for facile electron transfer.[5] Thus, a synergistic

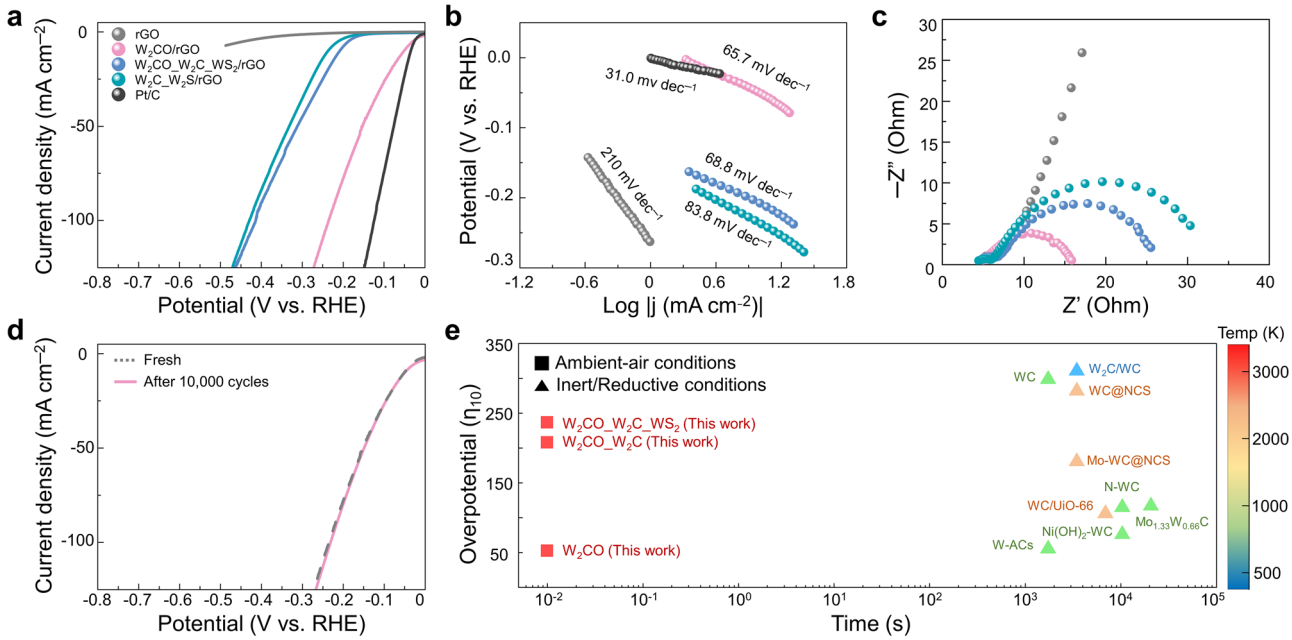

Figure 5. Hydrogen evolution reaction (HER) activity of TMDs and TMCs on rGO. a,b) Polarization curves (a) and Tafel plots of rGO, W_2CO/rGO, $W_2CO\_W_2C\_WS_2$/rGO, $W_2C\_WS_2$/rGO, and commercial Pt/C catalyst (b). c) Nyquist plot of EIS response at −0.20 V versus RHE. d) Polarization curve of W_2CO/rGO freshly prepared and after 10 000 CV cycles showing no significant overpotential increase. e) Comparison of the HER overpotentials regarding synthetic process time with recently reported tungsten carbides in the literature. The color in the Figure indicates the synthesis temperature corresponding to the right colormap. The exact synthetic and reaction conditions are summarized in Table S3 (Supporting Information).

effect of the heterostructure of α-MoC@MoS_2/rGO facilitates the surface reaction with NO_2 gas and the electron transfer, helping with recovery characteristics (Figure 4c–e). The ppb-scale limit of detection (LOD) and low deviation over 13 cyclic tests highlight their potential applicability for NO_2 monitoring in practical settings (Figure 4e; Figures S23 and S24, Supporting Information). Moreover, the rGO-based sensors exhibited excellent selectivity toward 5 ppm NO_2, compared to 5 ppm CH_3COCH_3, NH_3, C_7H_8, C_8H_{10}, CO, and C_2H_5OH analytes (Figure 4f). To elucidate the mechanism of NO_2 on the surface of α-MoC@MoS_2/rGO, we conducted ex situ XPS analyses to examine the N spectra after exposure to NO_2. The NO_2 molecules adsorbed on the surface of rGO, reacting with radicals or oxygen species to form hole-accumulation regions (Equations 1—3, Figure 4g).[47] Due to their localized nano-curvature, the core@shell structured NPs gained catalytically active lattice strain effects. Figure 4h shows that the lattice tensile strain in α-MoC@MoS_2/rGO was calculated to be ≈3.28% (0.274 to 0.283 nm). The lattice strain could contribute to an increase in active sites for NO_2 adsorption, leading to a high response toward NO_2 in α-MoC@MoS_2/rGO compared to rGO.[48]

$$NO_{2(ads)} + e^- \rightarrow NO^-_{2(ads)} \quad (1)$$

$$NO_{2(ads)} + O^-_{2(ads)} + 2e^- \rightarrow 2NO^-_{2\,ads} + 2O^-_{2(ads)} \quad (2)$$

$$NO_{2(ads)} + 2O^-_{(ads)} + e^- \rightarrow 2NO^-_{2\,ads} + 2O^{2-}_{(ads)} \quad (3)$$

To unveil the origin of the high catalytic activity of α-MoC@MoS_2/rGO-based NO_2 sensing, we conducted ex situ XPS analysis after exposures of 5 ppm NO_2 (Figure 4i). While the pristine rGO did not show noticeable changes upon exposure to NO_2, the α-MoC@MoS_2/rGO exhibited an emergence of an additional peak. After NO_2 exposure, numerous NO_2 molecules reacted strongly with rGO, as indicated by a new peak at 396.9 eV corresponding to Mo—N.[49,50] The α-MoC@MoS_2 plays the role of sensitizer for the NO_2 reaction on the surface of rGO. The core@shell heterostructured TMD NPs improved gas sensing performances for various core additives (e.g., Ag, Au, Fe_2O_3, In_2O_3, and Co_3O_4) and the other combinations, including the WS_2 (Figures S25 and S26, Supporting Information). These results demonstrate the strain effect derived from the core@shell structure, enhances the sensing performance of rGO sensing layers.

The growing demand for clean energy solutions has highlighted the need for efficient and durable electrocatalysts.[51] While platinum remains the most effective catalyst for the hydrogen evolution reaction (HER), its high cost and scarcity hinder large-scale implementation. Notably, WS_2 and tungsten carbides (W_2C, W_2CO) have been considered promising candidates to enhance the electrocatalytic HER activity, a technologically crucial component of water-splitting owing to their similar catalytic behavior to that of platinum. The electrocatalytic performance was confirmed under acidic conditions using a three-electrode rotating ring disk electrode system (Figure S27, Supporting Information). The polarization curves obtained by linear sweep voltammetry (LSV) reveal that pristine rGO exhibits an almost plateau-like behavior, indicating its inert HER catalytic activity (**Figure 5a**). Heightened HER activity was observed in tungsten compounds on rGO in stark contrast to pristine rGO. In fact, W_2CO/rGO, $W_2CO\_W_2C\_WS_2$/rGO, and $W_2C\_WS_2$/rGO show high HER activity, with overpotentials at 10 mA cm^{-1}

(50.5 mV, 207 mV, and 236 mV, respectively). To gain deeper insight into the HER kinetics, Tafel slopes were determined from the LSV data (Figure 5b). The W_2CO/rGO exhibits a Tafel slope of 65.7 mV dec^{-1}, suggesting it undergoes the Volmer-Heyrovsky mechanism, with the hydrogen adsorption step as the rate-determining step.[52] Similarly, $W_2CO\_W_2C\_WS_2$/rGO (68.8 mV dec^{-1}), $W_2C\_WS_2$/rGO (83.8 mV dec^{-1}) also follow Volmer-Heyrovsky mechanism, among them W_2CO/rGO showed the fastest HER kinetics.

Rapid HER kinetics were further supported by electrochemical impedance spectroscopy (EIS) data. Nyquist plots were plotted and fitted using a simple equivalent circuit (Figure 5c; Figure S28, Supporting Information). All catalysts exhibit two semicircles, which are attributed to electrode porosity and charge transfer resistance (Table S2, Supporting Information).[53] The W_2CO/rGO showed the lowest charge-transfer resistance (R_{ct}) of 9.7 Ω, much lower than that of $W_2CO\_W_2C\_WS_2$/rGO (19.8 Ω) and $W_2C\_WS_2$/rGO (26.5 Ω). These results indicate that the electrons received by the electrode were quickly transferred to the TMCs through the electroconductive rGO, enabling instantaneous charge transfer to the hydrogen ion and adsorbed hydrogen on the TMCs, which significantly enhanced the HER kinetics. With intrinsic catalytic activity, double-layer capacitance (C_{dl}) is an important parameter in determining the electrochemical surface area of an electrocatalyst (Figure S29, Supporting Information). From the scan rate and current densities from different cyclic voltammetry (CV) curves (Figure S29a–c, Supporting Information), we determined that the W_2CO/rGO exhibits a C_{dl} of 11.3 mF cm^{-2}, which is approximately twice as large as that of $W_2CO\_W_2C\_WS_2$/rGO (5.7 mF cm^{-2}) and $W_2C\_WS_2$/rGO (5.5 mF cm^{-2}) (Figure S29d, Supporting Information). These results revealed that the decomposition of ATTT and the carbothermic reaction of GO during the FTS facilitated the formation of small and uniform nuclei of tungsten carbides (i.e., W_2C, W_2CO), which led to a significant increase in the number of electrochemical reaction sites.[54,55] Lastly, for the electrocatalyst to be viable for water-splitting applications, it must also exhibit long-term durability. In this sense, an accelerated durability test was performed by conducting repetitive CV cycles between 0 and −0.2 V versus RHE with a scan rate of 50 mV s^{-1}. Remarkably, even after 10 000 CV cycles, the polarization curve of W_2CO/rGO showed no significant increase in the overpotential (Figure 5d). To highlight the ability to fabricate metastable highly active tungsten-based materials (i.e., W_2CO and W_2C) under extremely short process times (within 10 ms) by FTS, we compared the overpotential data of the tungsten carbides at 10 mA cm^{-2} for HER with recently reported literature values (Figure 5e; Table S3, Supporting Information). Our FTS-based synthetic platform, combined with precise control over reaction time, temperature, composition, and atmosphere, enables the efficient synthesis of complex nanostructures such as α-MoC@MoS_2 and metastable phases of W_2C and W_2CO. These materials, with their unique structural and catalytic properties, hold great potential for specific applications, paving the way for broader innovations in these fields. In perspective, the application-targeted metastable nanomaterials can be synthesized through our FTS methods with a facile one-step process, yielding highly effective catalytic sites for HER and gas sensor applications.

3. Conclusion

In conclusion, we demonstrated the heterostructure- and phase-engineering of TMDs and TMCs in an ambient air atmosphere using flash-thermal shock. This process features the synthesis of phase-controlled TMDs, carbothermic-reacted TMCs, and various combinations of core@shell NPs. In a standard synthesis, a single irradiation of intense pulsed light induces flash-thermal shock (1768–3162 K with 10 ms) of the precursor mixture with the aid of photothermal agents of GO. The metastable phase TMDs (1T-MoS_2, 1T-WS_2) and mixed-phase TMDs (1T- and 2H-MoS_2) were synthesized by controlling photothermal temperatures. In addition, the FTS triggered the carbothermic reaction of the GO, enabling the metastable carbon-based nanomaterials, including TMCs, TMC@TMD, and TMC@C. Furthermore, we demonstrated that various types of materials, including single-metal (Ag, Au), multielement/high entropy alloy (Pt-PdIrRuAu, PtPdIrRuAuCoSnNiFeCu), and transition metal oxide (Co_3O_4, In_2O_3, Fe_2O_3, and WO_3) NPs could serve as the core for the nucleation and growth of a curved TMD shell. To demonstrate the practical viability of the synthesized products for various applications, we developed i) a superior room-temperature NO_2 sensor in the form of α-MoC@MoS_2/rGO and ii) a promising HER catalyst in the form of W_2CO/rGO. Specifically, the α-MoC@MoS_2/rGO exhibited 8.7-fold enhanced room-temperature NO_2 gas sensing performance compared to pristine rGO, while the W_2CO/rGO showed low overpotentials of 50.5 mV with Tafel slopes of 65.7 mV dec^{-1}. Altogether, the phase- and heterostructure-controlled synthesis using the FTS method is a powerful and versatile synthetic method with products tailorable to various impactful applications such as gas sensing and water splitting.

4. Experimental Section

Materials: Graphene oxide dispersed DI solution (4 mg mL^{-1}), ammonium tetrathiomolybdate (ATTM), ammonium tetrathiotungstate (ATTT), silver, gold, cobalt(II, III) oxide, iron(II, III) oxide, tungsten oxide, and indium oxide particles, K_2PdCl_4, $HAuCl_4{\bullet}3H_2O$, $RuCl_3$, $IrCl_3$, $H_2PtCl_6{\bullet}6H_2O$, $CoCl_2{\bullet}6H_2O$, $NiCl_2{\bullet}6H_2O$, $CuCl_2{\bullet}2H_2O$, $SnCl_2{\bullet}2H_2O$, $FeCl_2{\bullet}4H_2O$ were purchased from Sigma–Aldrich Korea. Chemicals were used without purification.

Sample Preparation: For the synthesis of TMDs and TMCs on rGO using IPL treatment, we prepared GO solutions with different amounts of ATTM/ATTT (×:× GO:ATTM was indicated weight ratio of GO and ATTM). First, we added 5, 10, and 40 mg of ATTM to the 2.5 mL of GO solutions (10 mg), which indicated 2:1, 1:1, and 1:4 GO:ATTM, respectively, and the solutions were stirred for 3 h and ultrasonicated for an hour to disperse uniformly. The ATTM/GO solution (100 µL) was dropped onto a glass substrate (microslide glass, 76 × 52 × 1.2 mm) using a micropipette and then dried on a hot plate at 353.15 K for 1 h. The ATTT contained GO was consistent with the aforementioned methods except for the weight ratio (4:1, 2:1, and 1:1 GO:ATTT). For the seed-material@TMDs sample preparation, the additives were added 1 wt% for 1:1 GO:ATTM(ATTT). For the HEA@TMDs, 0.2 at% of K_2PdCl_4, $HAuCl_4{\bullet}3H_2O$, $RuCl_3$, $IrCl_3$, $H_2PtCl_6{\bullet}6H_2O$ (total 1 at%), and 0.1 at% of K_2PdCl_4, $HAuCl_4{\bullet}3H_2O$, $RuCl_3$, $H_2PtCl_6{\bullet}6H_2O$, $IrCl_3$, $CoCl_2{\bullet}6H_2O$, $NiCl_2{\bullet}6H_2O$, $CuCl_2{\bullet}2H_2O$, $FeCl_2{\bullet}4H_2O$, $SnCl_2{\bullet}2H_2O$ (total 1 at%) precursors were mixed with 1:1 GO:ATTM solutions. The sample coating and drying steps were consistent with the GO:ATTM(ATTT) systems.

IPL System: The Intense Pulsed Light (IPL) system contains five key components: a simmer board, xenon lamp, capacitors, a DC power supply, an insulated-gate bipolar transistor (IGBT), and IR sensor systems (Figure S30, Supporting Information). The xenon lamp irradiated the intensive pulsed light with a wavelength spectrum between 300–1000 nm (Figure S31, Supporting Information). To activate the xenon lamp, the simmer board initiates ignition, resulting in the streamer breakdown. Subsequently, the capacitors, powered by the DC power supply, are charged to the specified voltage (ranging from 0 to 500 V) and then discharged via the IGBT, creating an arc breakdown that produces a flashlight, which induces the photothermal effects of materials. Light power density can be modified by adjusting variables such as the applied voltage, pulse duration, pulse count, and the distance between the lamp and the sample. The energy of intensive light was measured by laser power meters (NOVA II, Ophir). The glass substrates were located 4 cm from the xenon lamp. The IPL system was irradiated on the substrate during 10 ms with high energy density (10, 25 J cm^{-2}).

Photothermal Temperature of GO Under IPL Irradiations: The IR sensor systems are introduced to detect the target temperature during the IPL process. The elaborate low temperature detected IR sensor (CTlaser 3MH2, Optris) detects from 473.15 to 1773.15 K, and the high temperature detected IR sensor (ther-moMETER CTRatio CTRM-2H1SF100-C3 from Micro-Epsilon) detects from 773.15 to 3273.15 K. These sensors produce a focused dot to measure the sample temperature, with samples positioned at the proper distance (15 cm). The measured analog signals are converted to digital signals by a data acquisition board (NI USB-6341 X series Multifunction DAQ, National Instruments). Since the temperature data were obtained with the emissivity value of the IR sensor at 1.00, these data were revised using tabulated values for the emissivity of graphene oxide ($\epsilon_{corrected} = 0.79$).[56] The following equation (Equation 4) was used for all samples to calculate the revised temperature data.

$$\frac{1}{T_{measured}} = \frac{1}{T_{corrected}} + \frac{\lambda \ln\left(\frac{\epsilon_{measured}}{\epsilon_{corrected}}\right)}{C_2} \quad (4)$$

In this equation, $T_{measured}$ represents the raw temperature data obtained from the sample, where the emissivity $\epsilon_{measured}$ was set to 1.00 by the infrared (IR) sensor. $T_{corrected}$ was the temperature corrected for the actual emissivity of tungsten oxide. The term λ denotes the detection wavelength of the IR sensor, which was 2.3 µm for the CTlaser and 1.5 µm for the CTRatio. Lastly, C_2 was the second radiant constant, with a value of µm K^{-1}.

Material Characterization: Transmission electron microscopy (TEM), scanning transmission electron microscopy (STEM), and elemental analysis (energy-dispersive X-ray spectroscopy (EDS)) were conducted by transmission electron microscopy (Thermo Fisher, Talos F200X G2). EDS mapping data were processed with Velox software (Thermo Fisher). The crystal structures were carried out using a powder X-ray diffractometer (XRD) (Rigaku, D/MAX-RC 12 kW) using Cu Kα ($\lambda = 1.54$ Å) radiation. The chemical elements and bonding states were analyzed using X-ray photoelectron spectroscopy (XPS) (Sigma Probe, Thermo VG Scientific) with Al Ka radiation (1486.7 eV). The zeta potential was measured with a particle size analyzer (Anton Paar, Litesizer 500).

Gas Sensing Measurements: The sensing materials, rGO samples, were initially coated to the Al_2O_3 substrate using the drop-coating method. Each sensing material was dispersed in ethanol (2 mg in 100 µL) and drop-coated onto the substrate using a micropipette (2.5 µL) several times at room temperature. Gas sensing tests were conducted in a homemade gas sensing system featuring a 16-channel multiplexer (34902A, Agilent), a data acquisition system (34972A, Agilent) that measured resistance across 16 channels at 4-s intervals, and a mass flow control system for regulating gas concentration. Sensing tests were conducted in a humid environment (15%, 55%, and 80% RH), controlled by a mixture of water bubbler and balancing gas with mass flow controllers. Sensitivity, selectivity, and durability tests involved cyclic on/off exposures (30 and 60 min) to various gases and air, with response calculated as the change in resistance ($\Delta R/R_{air}$ [%]), indicating the ratio of baseline resistance in the air (R_{air}) to resistance change after gas exposure. The baseline resistances were stabilized over 3 h at room temperature. The ex situ XPS was conducted with the sensing materials after exposure for 60 min toward 5 ppm of NO_2. The sensor substrates consist of three main components: an alumina board, gold electrodes, and a platinum heater. The alumina substrate measures 2.5 mm × 2.5 mm with a thickness of 0.2 mm and printed interdigitated Au electrodes (width: 25 µm, spacing: 70 µm) on the front side and a Pt heater on the backside. Connected via a four-pin system with Pt wires, two electrode pins measure the resistance, while the remaining two pins connect to the Pt heater to monitor the operating temperature.

Electrochemical Hydrogen Evolution Reaction Catalytic Activity Test: All electrochemical measurements were performed using a conventional three-electrode system with a rotating disk electrode rotator. A glassy carbon rotating disk electrode (RDE) with an active area of 0.196 cm^2, a graphite rod electrode, and an Ag/AgCl electrode were used as working electrode, counter electrode, and reference electrode, respectively. 4 mg of samples were uniformly dispersed in a mixture of 1 mL DI/IPA solution (3:1, v/v) with 80 µL of Nafion 117 containing solution (5 wt.%) using an ultrasonic bath to obtain electrocatalyst ink. After complete dispersion, 14 µL of dispersion (loading: 0.265 mg cm^{-2}) was carefully drop-coated on the RDE and dried for 2 h at 313.15 K. These experiments were conducted in a 0.5 M H_2SO_4 electrolyte purged with N_2 gas for 20 min before the test to evaluate the HER activity under acidic conditions. The potential was calibrated against the reversible hydrogen electrode (RHE) using the following equation:

$$E_{RHE} = E_{Ag/AgCl} + 0.059 \times pH + 0.197 \quad (5)$$

where the value of 0.197 was obtained by calibrating the Ag/AgCl electrode with a saturated KCl solution against the RHE. The polarization curve was obtained by linear sweep voltammetry (LSV) over a potential range of 0 to −0.7 V versus Ag/AgCl at a scan rate of 5 mV s^{-1}. The overpotential was determined based on the potential at which a current density of 10 mA cm^{-2} was reached. Electrochemical impedance measurement was performed in the frequency range from 1 м Hz to 0.1 Hz at a −0.20 V versus RHE with an amplitude of 5 mV. All electrochemical test data was reported without *iR* compensation.

Supporting Information

Supporting Information is available from the Wiley Online Library or from the author.

Acknowledgements

This work was supported by the National Research Foundation of Korea (NRF) grant funded by the Korea government (MSIT) (No. RS-2024-00435493). This work was also supported by the National Research Foundation of Korea grant funded by the Korea government, Ministry of Science and ICT (Development of Nanofiber Yarn Based Compound Sensor as a Comprehensive Wearable Healthcare Solution) (Grant No. RS-2024-00357296). This work was also supported by the National Research Foundation of Korea grant funded by the Korea government (MSIT) (No. RS-2023-00222411). This work was also supported by the National Research Foundation of Korea grant funded by the Korea government (MSIT) (No. RS-2023-00236572).

Conflict of Interest

The authors declare no conflict of interest.

Author Contributions

I.-D.K. supervised the overall project. E.S. conceived the work, designed the whole project, including conceptualization and experiments, and wrote

the manuscript. D.-H.K. contributed to the conceptualization. S.H.P. and S.-Y.C. assisted the IPL process. M.S. helped with the electrochemical measurements. J.C. and J.M.Y. carried out TEM measurements. J.A., J.W.B., and Y.C. assisted with materials synthesis and discussion. S.W. and M.K. helped to carry out gas sensing measurements. S.-J.C., S.-J.K., and J.L. contributed to the analysis discussion and edited the manuscript. All authors discussed the results and assisted during manuscript preparation.

Data Availability Statement

Research data are not shared.

Keywords

core@shell heterostructure, intense pulsed light, photothermal effect, transition metal carbides, transition metal dichalcogenides

Received: December 17, 2024
Revised: April 30, 2025
Published online:

[1] S. Manzeli, D. Ovchinnikov, D. Pasquier, O. V. Yazyev, A. Kis, *Nat. Rev. Mater.* **2017**, *2*, 17033.
[2] M. Chhowalla, H. S. Shin, G. Eda, L.-J. Li, K. P. Loh, H. Zhang, *Nat. Chem.* **2013**, *5*, 263.
[3] H. Xia, Z. Shi, C. Gong, Y. He, *J. Mater. Chem. A* **2022**, *10*, 19067.
[4] A. Castellanos-Gomez, R. Roldán, E. Cappelluti, M. Buscema, F. Guinea, H. S. Van Der Zant, G. A. Steele, *Nano Lett.* **2013**, *13*, 5361.
[5] A. P. Tiwari, Y. Yoon, T. G. Novak, A. Azam, M. Lee, S. S. Lee, G. h. Lee, D. J. Srolovitz, K. S. An, S. Jeon, *Adv. Mater. Interfaces* **2019**, *6*, 1900948.
[6] R. Wu, H. Zhang, H. Ma, B. Zhao, W. Li, Y. Chen, J. Liu, J. Liang, Q. Qin, W. Qi, *Chem. Rev.* **2024**, *124*, 10112.
[7] H. Zhu, G. Gao, M. Du, J. Zhou, K. Wang, W. Wu, X. Chen, Y. Li, P. Ma, W. Dong, *Adv. Mater.* **2018**, *30*, 1707301.
[8] Y. Guo, J. Li, X. Zhan, C. Wang, M. Li, B. Zhang, Z. Wang, Y. Liu, K. Yang, H. Wang, *Nature* **2024**, *630*, 346.
[9] M. Kim, Y. Kim, M. Y. Ha, E. Shin, S. J. Kwak, M. Park, I. D. Kim, W. B. Jung, W. B. Lee, Y. Kim, *Adv. Mater.* **2023**, *35*, 2211497.
[10] W. Chen, Z. Wang, K. V. Bets, D. X. Luong, M. Ren, M. G. Stanford, E. A. McHugh, W. A. Algozeeb, H. Guo, G. Gao, *ACS Nano* **2021**, *15*, 1282.
[11] S. Park, A. Lee, K.-H. Choi, S.-K. Hyeong, S. Bae, J.-M. Hong, T.-W. Kim, B. H. Hong, S.-K. Lee, *ACS Nano* **2020**, *14*, 8485.
[12] B. Wang, C. Wang, X. Yu, Y. Cao, L. Gao, C. Wu, Y. Yao, Z. Lin, Z. Zou, *Nature Synthesis* **2022**, *1*, 138.
[13] X. Zheng, X. Gao, R. A. Vilá, Y. Jiang, J. Wang, R. Xu, R. Zhang, X. Xiao, P. Zhang, L. C. Greenburg, *Nat. Nanotechnol.* **2023**, *18*, 153.
[14] D.-H. Kim, J.-H. Cha, G. Shim, Y. H. Kim, J.-S. Jang, H. Shin, J. Ahn, S.-Y. Choi, I.-D. Kim, *Chem* **2022**, *8*, 1014.
[15] J. H. Cha, D. H. Kim, C. Park, S. J. Choi, J. S. Jang, S. Y. Yang, I. D. Kim, S. Y. Choi, *Adv. Sci.* **2020**, *7*, 1903318.
[16] A. Abdelhafiz, A. N. M. Tanvir, M. Zeng, B. Wang, Z. Ren, A. R. Harutyunyan, Y. Zhang, J. Li, *Adv. Sci.* **2023**, *10*, 2300426.
[17] B. Deng, L. Eddy, K. M. Wyss, C. S. Tiwary, J. M. Tour, *Nat. Rev. Clean Techno.* **2025**, *1*, 32.
[18] M. Aykol, S. S. Dwaraknath, W. Sun, K. A. Persson, *Sci. Adv.* **2018**, *4*, aaq0148.
[19] B. Deng, Z. Wang, W. Chen, J. T. Li, D. X. Luong, R. A. Carter, G. Gao, B. I. Yakobson, Y. Zhao, J. M. Tour, *Nat. Commun.* **2022**, *13*, 262.
[20] E. Shin, D.-H. Kim, J.-H. Cha, S. Yun, H. Shin, J. Ahn, J.-S. Jang, J. W. Baek, C. Park, J. Ko, *ACS Nano* **2022**, *16*, 18133.
[21] J. H. Cha, S. H. Cho, D. H. Kim, D. Jeon, S. Park, J. W. Jung, I. D. Kim, S. Y. Choi, *Adv. Mater.* **2023**, *35*, 2305222.
[22] S. J. Choi, J. S. Jang, H. J. Park, I. D. Kim, *Adv. Funct. Mater.* **2017**, *27*, 1606026.
[23] S. J. Choi, S. J. Kim, J. S. Jang, J. H. Lee, I. D. Kim, *Small* **2016**, *12*, 5826.
[24] A. Serrano-Lotina, R. Portela, P. Baeza, V. Alcolea-Rodríguez, M. Villarroel, P. Ávila, *Catal. Today* **2023**, *423*, 113862.
[25] Y. Shen, V. Boffa, I. Corazzari, A. Qiao, H. Tao, Y. Yue, *Carbon* **2018**, *138*, 337.
[26] B. Gupta, N. Kumar, K. Panda, V. Kanan, S. Joshi, I. Visoly-Fisher, *Sci. Rep.* **2017**, *7*, 45030.
[27] L. Sygellou, *Appl. Surf. Sci.* **2019**, *476*, 1079.
[28] T. A. Loh, D. H. Chua, A. T. Wee, *Sci. Rep.* **2015**, *5*, 18116.
[29] D. Zhang, T. Liu, J. Cheng, Q. Cao, G. Zheng, S. Liang, H. Wang, M.-S. Cao, *Nano-Micro Lett.* **2019**, *11*, 1.
[30] S. Shi, Z. Sun, Y. H. Hu, *J. Mater. Chem. A* **2018**, *6*, 23932.
[31] U. Gupta, B. Naidu, U. Maitra, A. Singh, S. N. Shirodkar, U. V. Waghmare, C. Rao, *APL Mater.* **2014**, *2*, 092802.
[32] H. Liu, W. Shi, Y. Guo, Y. Mei, Y. Rao, J. Chen, S. Liu, C. Lin, A. Nie, Q. Wang, *ACS Nano* **2024**, *18*, 29724.
[33] V. Mehta, H. S. Saini, S. Srivastava, M. K. Kashyap, K. Tankeshwar, *J. Mater. Sci.* **2022**, *57*, 10702.
[34] A. Kurlov, A. Gusev, *Inorg. Mater.* **2006**, *42*, 121.
[35] X. Zhao, X. Ma, J. Sun, D. Li, X. Yang, *ACS Nano* **2016**, *10*, 2159.
[36] J. G. DiStefano, Y. Li, H. J. Jung, S. Hao, A. A. Murthy, X. Zhang, C. Wolverton, V. P. Dravid, *Chem. Mater.* **2018**, *30*, 4675.
[37] J. G. DiStefano, A. A. Murthy, S. Hao, R. D. Reis, C. Wolverton, V. P. Dravid, *Nanoscale* **2020**, *12*, 23897.
[38] Y. Li, M. Majewski, S. Islam, S. Hao, A. Murthy, J. DiStefano, E. Hanson, Y. Xu, C. Wolverton, M. Kanatzidis, M. R. Wasielewski, X. Chen, V. P. Dravid, *Nano Lett.* **2018**, *18*, 7104.
[39] S.-Y. Cho, J. Y. Kim, O. Kwon, J. Kim, H.-T. Jung, *J. Mater. Chem. A* **2018**, *6*, 23408.
[40] S. Y. Park, J. E. Lee, Y. H. Kim, J. J. Kim, Y.-S. Shim, S. Y. Kim, M. H. Lee, H. W. Jang, *Sens. Actuators, B* **2018**, *258*, 775.
[41] E. Vorobyeva, E. Fako, Z. Chen, S. M. Collins, D. Johnstone, P. A. Midgley, R. Hauert, O. V. Safonova, G. Vile, N. Lopez, S. Mitchell, J. P. Ramirez, *Angew. Chem., Int. Ed.* **2019**, *58*, 8724.
[42] K. Liu, P. Yang, S. Li, J. Li, T. Ding, G. Xue, Q. Chen, G. Feng, J. Zhou, *Angew. Chem., Int. Ed.* **2016**, *55*, 8003.
[43] Y.-M. Jo, D.-H. Kim, J. Wang, J. J. Oppenheim, M. Dincaˇ, *J. Am. Chem. Soc.* **2024**, *146*, 20213.
[44] G. Santarossa, K. Hahn, A. Baiker, *Langmuir* **2013**, *29*, 5487.
[45] H.-Y. Li, C.-S. Lee, D. H. Kim, J.-H. Lee, *ACS Appl. Mater. Interfaces* **2018**, *10*, 27858.
[46] R. R. Kumar, M. R. Habib, A. Khan, P.-C. Chen, T. Murugesan, S. Gupta, A. K. Anbalagan, N.-H. Tai, C.-H. Lee, H.-N. Lin, *ACS Appl. Nano Mater.* **2021**, *4*, 9459.
[47] H. Bai, H. Guo, J. Wang, Y. Dong, B. Liu, Z. Xie, F. Guo, D. Chen, R. Zhang, Y. Zheng, *Sens. Actuators, B* **2021**, *337*, 129783.
[48] Y. Linghu, C. Wu, *J. Phys. Chem. C* **2019**, *124*, 1511.
[49] Z. Guo, Y. Zhong, Z. Xuan, C. Mao, F. Du, G. Li, *RSC Adv.* **2015**, *5*, 62624.
[50] J. Cho, H. Seok, I. Lee, J. Lee, E. Kim, D. Sung, I.-K. Baek, C.-H. Lee, T. Kim, *Sci. Rep.* **2022**, *12*, 10335.
[51] Y. Cao, *ACS Nano* **2021**, *15*, 11014.
[52] Q. Tang, D. Jiang, *ACS Catal.* **2016**, *6*, 4953.
[53] Z. Shi, Y. Wang, H. Lin, H. Zhang, M. Shen, S. Xie, Y. Zhang, Q. Gao, Y. Tang, *J. Mater. Chem. A* **2016**, *4*, 6006.

[54] Y.-L. T. Ngo, K. Bhamu, A. Voronova, J. Jana, S. G. Kang, J. S. Chung, W. M. Choi, J. H. Jang, S. H. Hur, B. Seo, *Chem. Eng. J.* **2022**, *450*, 137915.
[55] X. Fan, H. Zhou, X. Guo, *ACS Nano* **2015**, *9*, 5125.
[56] G. Cui, Z. Peng, X. Chen, Y. Cheng, L. Lu, S. Cao, S. Ji, G. Qu, L. Zhao, S. Wang, *Adv. Sci.* **2022**, *9*, 2105004.